Dislocation modelling in Ti 2 AlN MAX phase based on the Peierls–Nabarro model

Karine Gouriet, Philippe Carrez, Patrick Cordier, Antoine Guitton, Anne Joulain, Ludovic Thilly, Christophe Tromas

Dislocation modelling in Ti_2AlN MAX phase based on the Peierls–Nabarro model

Karine Gouriet[a]*, Philippe Carrez[a], Patrick Cordier[a], Antoine Guitton[b], Anne Joulain[b], Ludovic Thilly[b] and Christophe Tromas[b]

[a]*Unité Matériaux et Transformation, CNRS UMR 8207, Université de Lille 1, Bat C6, 59655 Villeneuve d'Ascq, France;* [b]*Institut Pprime, CNRS Université de Poitiers, ENSMA, UPR 3346, 11 Boulevard Marie et Pierre Curie, BP 30179, F-86962 Futuroscope, France*

In this study, we determined the core structure and the Peierls stress of $\frac{1}{3}\langle 2\,\bar{1}\,\bar{1}\,0\rangle$ dislocations in Ti_2AlN MAX phase. We use a generalized Peierls–Nabarro model, called Peierls–Nabarro–Galerkin (PNG), coupled with first principles calculations of generalized stacking fault (GSF). The GSF calculations show that dislocation glide in the basal plane will occur preferentially between M (here Ti) and A (here Al) planes. Additionally, the results of PNG calculations demonstrate that whatever the dislocation character, $\frac{1}{3}\langle 2\,\bar{1}\,\bar{1}\,0\rangle$ dislocations are dissociated in the basal plane, with a dissociation distance below the experimental resolution of transmission electron microscopy observations. Finally, the Peierls stress calculations show that the edge and screw characters are the easiest characters to glide in the basal plane.

Keywords: MAX phase; dislocations; Peierls–Nabarro model

1. Introduction

MAX phases are a class of hexagonal ternary nitrides or carbides of general formula $M_{n+1}AX_n$ (n = 1–3), where M is a transition metal, A belongs to group IIIA to VIA and X is either carbon or nitrogen [1,2]. These materials present a nanolaminated structure with $M_{n+1}X_n$ layers interleaved with metallic A layers. If the first MAX phases have been synthesized in the 1970s, they have been brought into light in the 1990s by Barsoum and co-workers, who discovered their promising properties and synthesized many new MAX phases. There are nowadays about seventy known MAX phases which arouse a great interest since they exhibit an unusual combination of metals and ceramics properties, suggesting promising technological applications [3].

Among the specific characteristics of MAX phases, their mechanical properties are of particular interest. They are elastically stiff like their corresponding binary carbide or nitride, but they have rather low yield strength and are also readily machinable [1,4]. At high temperature, they present a brittle to ductile transition [3,5,6]. These mechanical properties are due to their nanolayered structure at room temperature; plastic deformation in MAX phases is mainly governed by basal slip, with dislocations arranging themselves in pile ups or in walls. In such configuration, two dislocation walls with opposite

*Corresponding author. Email: Karine.Gouriet@univ-lille1.fr

Burgers vectors define a kink band which is probably the key mechanism to explain the plastic deformation of MAX phases at room temperature.

However, recent results obtained by the compression test under confining pressure [7] and by nanoindentation [8] of MAX polycrystals showed that the idea of basal plane dislocations gliding freely in grains with no interaction is oversimplified. The understanding and the improvement of the mechanical properties of MAX phases are thus intrinsically linked to the knowledge of dislocation behaviour in these materials.

Very few transmission electron microscopy (TEM) dislocation analyses are reported in the literature for MAX phase. The first papers were focused on Ti_3SiC_2, which is probably the most studied MAX phase [5,9]. In this case, isolated low-angle tilt boundaries were characterized, but these studies were limited to short and straight dislocation segments. In as-grown Ti_4AlN_3, Joulain et al. [10] observed dislocation interactions and out of the basal plane dislocation segments. More recently, Guitton et al. [7] characterized the dislocation structures in Ti_2AlN deformed under confining pressure up to 5% plastic strain. Strain hardening was observed during the compression test, and the TEM analysis of the deformed sample revealed complex interaction between dislocations in the basal plane producing dislocation cells. Furthermore, the dislocation segments were found to be aligned along specific directions leading to screw, 30°, 60° or edge character. Such a configuration is presented in Figure 1, where long straight dislocation segments are observed. The segments represented in black have a pure edge character, while the segments drawn in grey have a 30° character. The preferential orientation of the dislocation lines in Ti_2AlN may be an evidence of lattice friction in this material. Here again, there is a need for a better understanding of the dislocation properties and their core structures in MAX phases. For this purpose, we propose here a theoretical approach based on the *ab initio* calculations of the elastic constants, of the generalized stacking fault (GSF) energy surfaces (also called γ-surfaces hereafter), and of the core energies and the Peierls stress for dislocations. As a first step, this study presents the calculation of the γ-surfaces of basal planes (0 0 0 1) in the MAX phase Ti_2AlN considering two different cutting levels (between N and Ti atomic layers, and between the Ti and Al atomic layers as described in the computational section). In view of these results, the dislocation core structures are examined in this material.

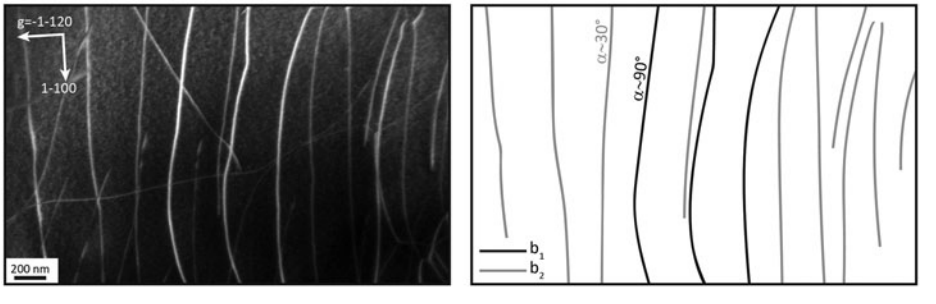

Figure 1. TEM observation of long straight dislocation segments lying in the basal plane in Ti_2AlN. Dislocations exhibit strong orientation dependence with segments having strong edge (in black on the right panel) and 30° (in grey on the right panel) characters with a Burgers vector $\mathrm{b} = \pm\frac{1}{3}\langle 1\,1\,\bar{2}\,0\rangle$.

2. Computational methods

The concept of γ-surfaces was introduced by Vitek [11] in the framework of the Peierls–Nabarro model giving access to the core structure of dislocations. The principle relies on the computation of the relaxed energy associated with any relative translation of the lattice with respect to a given shear plane. In the following, dislocation core structures are calculated with the Peierls–Nabarro–Galerkin [12] (PNG) model. As an input of the PNG model, we use γ-surfaces calculated from first principles calculations.

2.1. *Ground properties (*ab initio*) calculations*

First principles calculations have been performed based on the density functional theory within the generalized gradient approximation [13]. Calculations were performed using the VASP code [14–16] and the all-electron projector augmented-wave method [17,18]. The outmost core radii are 2.30 a.u. for Ti atoms, 1.9 a.u. for Al atoms and 1.5 a.u. for the N atoms. Namely, with the pseudo-potentials used in this work, 3p 4s 3d states for Ti, 2s 3p states for N and 2s 1p states for Al are treated as valence states. All calculations have been performed using a single cut-off energy value of 400 eV for the plane wave expansion and a Monkhorst–Pack grid [19] scheme was used for first Brillouin zone sampling.

The crystallographic structure of Ti_2AlN was optimized (full relaxation of cell parameters and of atomic positions) using a 16 × 16 × 8 K-point mesh, and the athermal elastic constant was determined from Hooke's Law $[\sigma] = [C][\varepsilon]$. For a hexagonal lattice, there are five independent elastic constants, usually referred to as C_{11} (=C_{22}), C_{12}, C_{13}, C_{33} and C_{44} (=C_{55}) [20] and the sixth elastic constant is given by $C_{66} = (C_{11} - C_{12})/2$. Then Hooke's Law is simplified:

$$\begin{pmatrix} \sigma_1 \\ \sigma_2 \\ \sigma_3 \\ \sigma_4 \\ \sigma_5 \\ \sigma_6 \end{pmatrix} = \begin{pmatrix} C_{11} & C_{12} & C_{13} & & & \\ C_{12} & C_{11} & C_{13} & & 0 & \\ C_{13} & C_{13} & C_{33} & & & \\ & & & C_{44} & 0 & 0 \\ & 0 & & 0 & C_{44} & 0 \\ & & & 0 & 0 & C_{66} \end{pmatrix} \begin{pmatrix} \varepsilon_1 \\ \varepsilon_2 \\ \varepsilon_3 \\ \varepsilon_4 \\ \varepsilon_5 \\ \varepsilon_6 \end{pmatrix}$$

These quantities were estimated by applying [21] a set of strains e with the third axis taken along the c axis. The five configurations used to obtain the elastic constants are given in Table 1.

2.2. *GSF energy calculations*

The simulation cells for all our studies use a Z coordinate normal to the glide plane. The supercell is built on three vectors which, in standard hexagonal crystallographic notation, we write as $X = [\bar{2}\,1\,1\,0]$, $Y = [1\,\bar{2}\,1\,0]$, $Z = [0\,0\,0\,1]$. We consider two different levels for shearing the basal plane of the crystal structure of Ti_2AlN (Figure 2): (1) between Al and Ti atoms and (2) between N and Ti atoms.

γ-surfaces are computed as follows. Atoms on surfaces along the Z direction are imposed fixed positions, and periodic boundary conditions are applied along X and Y. A

Table 1. Strain–stress configurations used for elastic constant determinations, given in terms of the strain variable ε. The last two strain configurations are applied on an orthorhombic mesh (the other are applied on the hexagonal mesh).

Strain tensor	Stress tensor	Elastic coefficients
$(\varepsilon \quad \varepsilon \quad 0 \quad 0 \quad 0 \quad 0)$	$(\sigma_1 \quad \sigma_2 \quad \sigma_3 \quad 0 \quad 0 \quad 0)$	$\sigma_1 = (C_{11} + C_{12})\varepsilon = \sigma_2, \sigma_3 = 2C_{13}\varepsilon$
$(\varepsilon \quad -\varepsilon \quad 0 \quad 0 \quad 0 \quad 0)$	$(\sigma_1 \quad \sigma_2 \quad 0 \quad 0 \quad 0 \quad 0)$	$\sigma_1 = (C_{11} - C_{12})\varepsilon = -\sigma_2$
$(0 \quad 0 \quad \varepsilon \quad 0 \quad 0 \quad 0)$	$(\sigma_1 \quad \sigma_2 \quad \sigma_3 \quad 0 \quad 0 \quad 0)$	$\sigma_1 = \sigma_2 = C_{13}\varepsilon, \sigma_3 = C_{33}\varepsilon$
$(0 \quad 0 \quad 0 \quad 0 \quad \varepsilon \quad 0)$	$(0 \quad 0 \quad 0 \quad 0 \quad \sigma_5 \quad 0)$	$\sigma_5 = 2C_{55}\varepsilon$
$(\varepsilon \quad 0 \quad \varepsilon \quad 0 \quad 0 \quad 0)$	$(\sigma_1 \quad \sigma_2 \quad \sigma_3 \quad 0 \quad 0 \quad 0)$	$\sigma_1 = (C_{11} + C_{13})\varepsilon,$ $\sigma_2 = (C_{12} + C_{13})\varepsilon, \sigma_3 = (C_{13} + C_{33})\varepsilon$

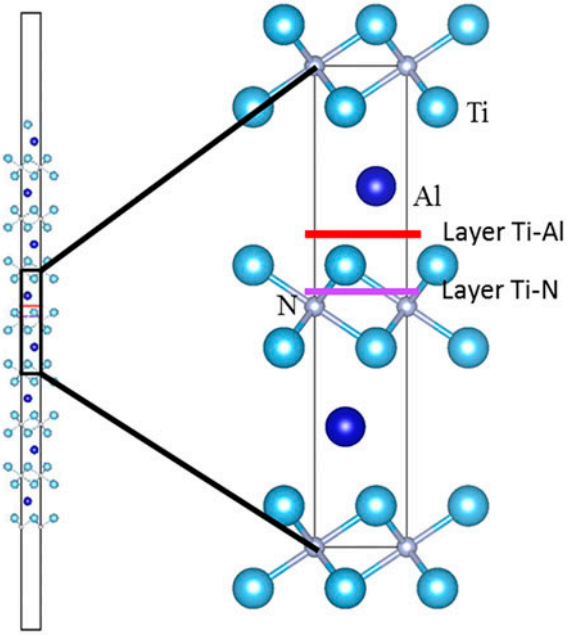

Figure 2. (colour online) Ti_2AlN structure and supercell used for the γ-surfaces calculations. The red line is the trace of (0 0 0 1) between Al and Ti layer. The purple line is the trace of (0 0 0 1) between N and Ti layer. Ti atoms are in cyan, Al in blue and N in grey. The zoom corresponds to the centre of the supercell and is equivalent to one unit cell.

vacuum buffer is added in the direction normal to the slip plane to avoid interaction between repeated stacking faults resulting from the use of periodic boundary conditions along Z. The upper half of the crystal ($Z > 0.5c$) is shifted by a translation vector $f = \delta_x X + \delta_y Y$ in the X–Y plane. All atoms are held fixed in the X and Y directions but are allowed to relax along the Z direction. The γ-surface then corresponds to the relaxed energy for any translation f within the shear plane. For *ab initio* calculations, perfect crystals of dimensions (1 × 1 × 4) unit cells are created for the basal planes.

2.3. *The PNG model*

In the PNG model, the dislocation core structure naturally emerges from the minimizing of an elastic energy and of an interplanar potential. Dislocation displacement fields are computed through an element-free Galerkin method. The non-linear behaviour is ensured by a displacement jump along potential glide planes of the structure associated with an extra cost in energy attributed to the interplanar potential. The latter is a function of the γ-surface energies from which the linear elastic part has been subtracted. As described in [22–24], a PNG calculation involves a nodal mesh, homothetic to the crystal structure, which incorporates γ-surfaces energies. Once a discrete Volterra dislocation is introduced into the volume, the equilibrium of displacement jump fields is determined through a viscous relaxation scheme. In the following, boundary conditions, consistent with a dislocation in an infinite media, are used by imposing a convolution of an elementary elastic solution with the dislocation density (see [22] for implementation details).

From energy considerations, Barsoum et al. [5] suggested that only basal dislocations play a role in the plastic behaviour of MAX phases. Due to the lattice anisotropy ($c/a = 4.5$) and the lamellar structure of Ti_2AlN (Figure 2), nucleation of dislocations is supposed to occur only in the basal plane. Furthermore, this slip system is observed in [7]. Then dislocation glide will occur in the basal plane with the Burgers vector $\frac{1}{3}\langle 2\,\bar{1}\,\bar{1}\,0\rangle$, which is the shortest lattice vector, the $\boldsymbol{a}$ generation vectors of the unit cell in the basal plane. Therefore, our PNG calculations will rely on a single γ-surface corresponding to the energy landscape associated with the basal plane.

Four different characters of dislocation are studied: screw, 30°, 60° and edge. PNG nodal meshes are built with respect to the *P63* symmetry of Ti_2AlN [21,25]. Two different meshes are thus used here, where the basal plane is in the (zOx) mesh plane, and the dislocation line along the z direction: one for the screw and 60° characters, and one for 30° and edge characters. For all calculations, meshes dimensions are equivalent to 40 MAX phase unit cells with a nodal resolution of 16 nodes per Burgers vector. Accordingly to [24], we check that increasing mesh dimensions or nodes number does not influence the results.

2.4. *Peierls stress calculations*

In the following, we define *S(x)* and *E(x)* the screw and edge disregistry components of the dislocation, with x-axis normal to the dislocation line. *S(x)* and *E(x)* are deduced from the nodal displacement of the PNG mesh. The local misfit energy density of the dislocation is then $\Gamma(x) = \gamma(S(x), E(x))$ [26,27]. Assuming that the misfit energy $E_{mis}(u)$ reflects the Peierls potential felt by a dislocation as a function of its position u, the associated Peierls stress can be defined as:

$$\sigma_p = max\left\{\frac{1}{b}\frac{dE_{mis}(u)}{du}\right\} \tag{1}$$

where b is the Burgers vector modulus. Based on the local misfit energy density [28], $E_{mis}(u)$ is thus calculated from the following discrete summation

$$E_{mis}(u) = \sum_m \gamma(S(ma' - u), E(ma' - u))a' \tag{2}$$

where a' is the periodicity of E_{mis}, taken as the shortest unit cell parameter in the direction of the dislocation's displacement.

3. Results

In this work, the structural optimization was first performed for the perfect Ti_2AlN crystal structure. The calculated lattice parameters and elastic constants are shown in Table 2. Our results are in good agreement with experimental and other theoretical values [21,25,29,30].

3.1. *γ-surface results*

The γ-surfaces of basal planes $(0\,0\,0\,1)$ obtained at two different cutting levels are shown in Figure 3. The γ-lines along $[\bar{2}\,1\,1\,0]$ and $[0\,\bar{1}\,1\,0]$ are shown in Figures 4 and 5, for a quantitative comparison of the ability of shearing the two levels. Shearing the Al–Ti layer is much easier whatever the direction. A stable stacking fault γ_s is observed at $\frac{1}{3}\langle 1\,\bar{1}\,0\,0\rangle$. As a consequence, we expect $\frac{1}{3}[\bar{2}\,1\,1\,0]$ dislocations to be dissociated with the dissociation path shown on Figure 3.

3.2. *Dislocation core structures*

Dislocation core structures are calculated by the PNG model using as an input the elasticity tensor and the $(0\,0\,0\,1)$ γ-surface corresponding to a shear between Ti and Al atoms.

For all dislocation characters (0° (screw), 30°, 60° or 90° (edge)), defined as the angle φ between the dislocation line direction and the Burgers vector, we introduce in the PNG model the (Ti–Al) basal plane which contains the $\frac{1}{3}[\bar{2}\,1\,1\,0]$ Burgers vector. Analysis of node displacement resulting from the relaxation of the dislocation core shows dissociation in two mixed components. The dissociation paths are identical for all dislocation characters and involve the stable stacking fault configuration at $\frac{1}{3}\langle 1\,\bar{1}\,0\,0\rangle$ as

Table 2. Lattice parameters in angstroms and elastic constants in GPa. The isotropic constants (E, G, B and ν) are calculated using the Voigt formalism [40].

	Present	Theory [21]	Theory [41]	Theory [25]	Theory [29]	Exp
a	3.00151	2.998		2.9504	2.9996	2.98846 [7]
c	13.6032	13.634		13.3954	13.6179	13.5917 [7]
$C_{11} = C_{22}$	313	309	342	311	312	
C_{33}	283	282	283	298	286	
$C_{44} = C_{55}$	128	125	123	133	125	
C_{12}	58	67	56	71	102	
C_{13}	88	90	96	76	93	
E	295	281	293		281	286 [30]
G	128	118	163		116	124 [30]
B	153	155	163		159	
ν	0.16		0.20		0.206	0.18 [30]

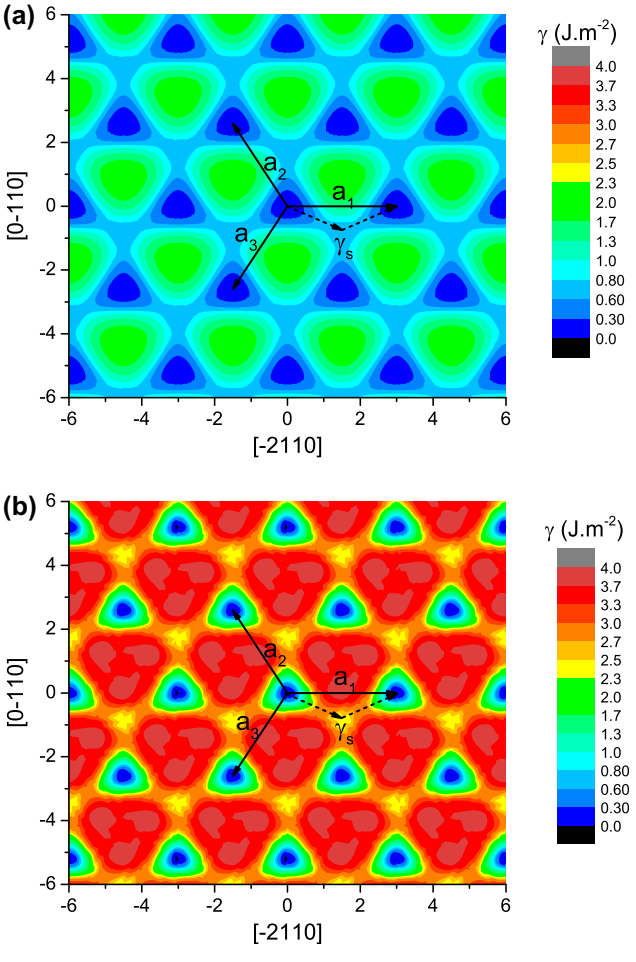

Figure 3. (colour online) γ-surfaces (in J/m²) in (0 0 0 1) with shear (a) between Ti and Al atoms and (b) between Ti and N atoms. The hexagonal base (a_1, a_2, a_3) is represented, γ_s is the stable stacking fault with (a) $\gamma_s = 0.72$ J/m² and (b) $\gamma_s = 2.06$ J/m². The dashed arrows represent the presumed dissociation path of the dislocation with the a_1 Burgers vector.

plotted on the γ-surface in Figure 6. For sake of consistency between the four characters, the core structure will be displayed as the disregistry function f:

$$f(x) = \sqrt{S^2 \cos^2 \varphi + E^2 \sin^2 \varphi} \tag{3}$$

Then, f is plotting as a function of the x-axis (Figures 7–10). Note that the core structure exhibits a wide spreading of 20 Å (i.e. approximately six times the modulus of the Burgers vector) in the basal plane. This tendency for core spreading is indicated by a shoulder on the disregistry curve, and in particularly for the edge dislocation which presents the larger width. As such a feature may indicate a tendency for dissociation, we

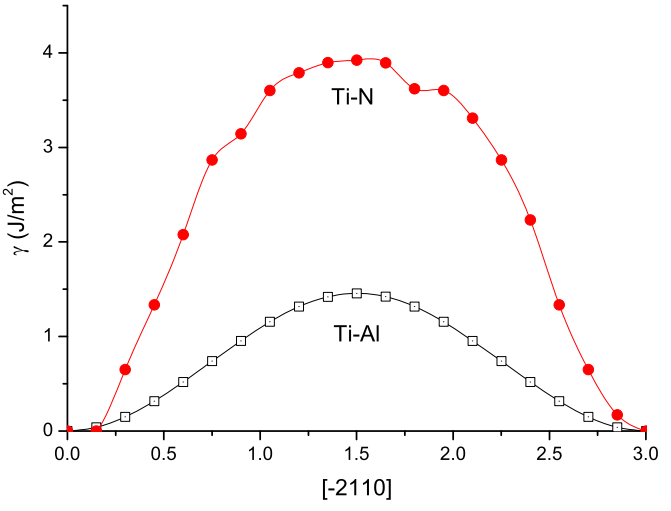

Figure 4. (colour online) γ-line along $[\bar{2}\,1\,1\,0]$ in $(0\,0\,0\,1)$. The black line and open square symbol corresponds to the (Ti–Al) layer, and the red line and circle symbol to the (Ti–N) layer.

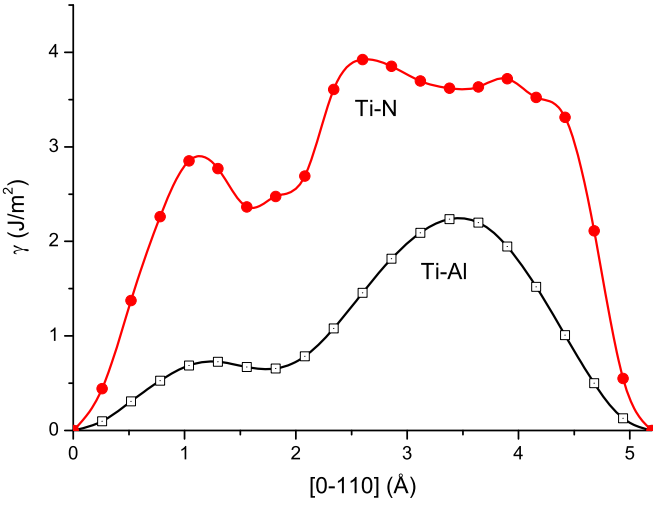

Figure 5. (colour online) γ-line along $[0\,\bar{1}\,1\,0]$ in $(0\,0\,0\,1)$. The black line and open square symbol corresponds to the (Ti–Al) layer, and the red line and circle symbol to the (Ti–N) layer.

performed a smooth fitting (Equation 4) of the disregistry functions using a sum of two atan functions [26,31].

$$f(x) = \frac{b}{2} + \frac{b}{\pi}\left(\alpha_1 \operatorname{atan}\left(\frac{x - x_1}{\zeta_1}\right) + \alpha_2 \operatorname{atan}\left(\frac{x - x_2}{\zeta_2}\right)\right) \tag{4}$$

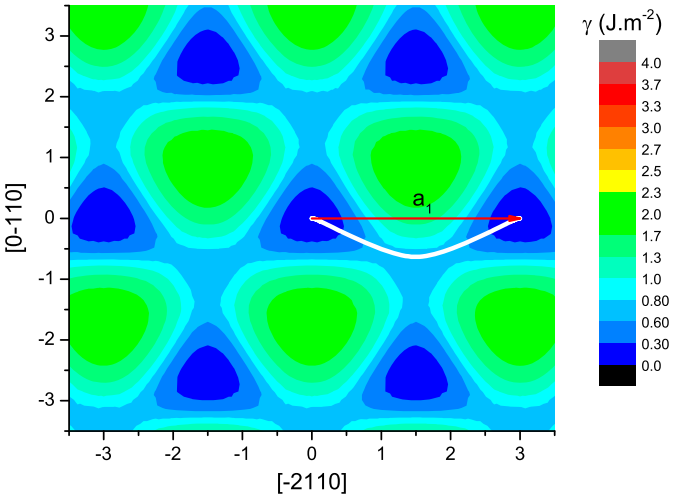

Figure 6. (colour online) γ-surfaces (in J/m²) in (0 0 0 1) plane between Ti and Al on which dissociation path (in white line and obtained with PNG calculation) of the $\frac{1}{3}\langle\bar{2}\,1\,1\,0\rangle$ dislocations has been superimposed. The $\frac{1}{3}\langle\bar{2}\,1\,1\,0\rangle$ Burgers vector is in red.

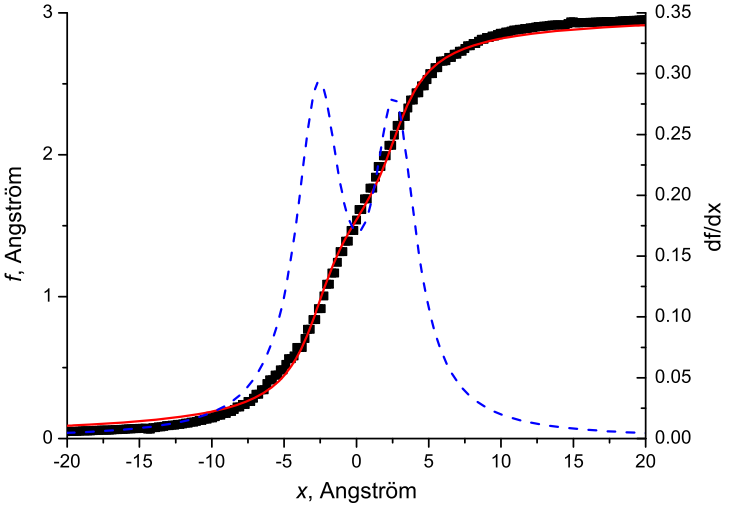

Figure 7. (colour online) Core structure of screw dislocation. Disregistry function *f(x)* and associated Burgers vector density $\rho = \mathrm{d}f(x)/\mathrm{d}x$ (dotted line) are plotted in (0 0 0 1) plane.

The parameters describing the calculated relaxed cores are given in Table 3. It turns out that the misfit distribution can be interpreted as two symmetric partial dislocations separated by a distance Δ (corresponding to x_1–x_2 in Equation 4). In each case, the separation distance between the two partials is below 7 Å (see Table 3). We observe that the separation distance increases with the angle between the Burgers vector and the dislocation line.

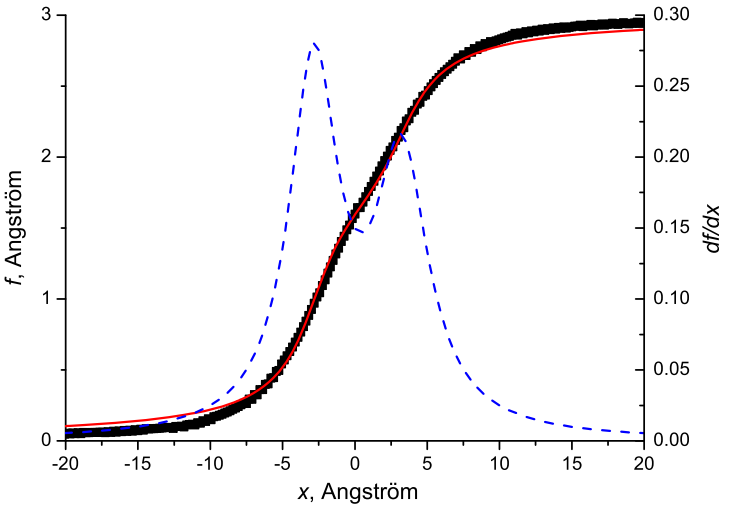

Figure 8. (colour online) Core structure of 30° dislocation. Disregistry function *f(x)* and associated Burgers vector density $\rho = \mathrm{d}f(x)/\mathrm{d}x$ (dotted line) are plotted in (0 0 0 1) plane.

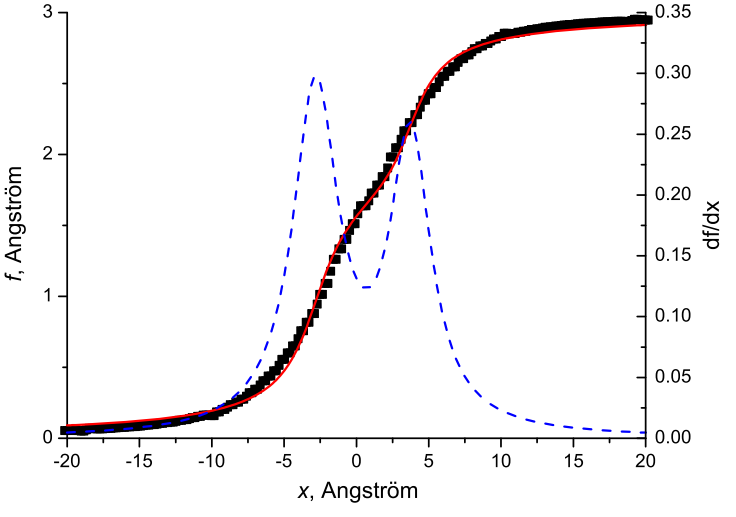

Figure 9. (colour online) Core structure of 60° dislocation. Disregistry function *f(x)* and associated Burgers vector density $\rho = \mathrm{d}f(x)/\mathrm{d}x$ (dotted line) are plotted in (0 0 0 1) plane.

Finally, the misfit energy $E_{mis}(u)$ and the Peierls stresses σ_p were determined using Equations (1) and (2). The four characters exhibit very comparable Peierls stresses, below 1 GPa. The results (given in Table 3) show two distinct cases: (i) the Peierls stress is the smallest and nearly the same for screw and edge characters and (ii) the 30° and 60° characters are about 50% harder than the screw and edge ones. The screw character appears thus to be the easiest character to glide in the basal plane. On the

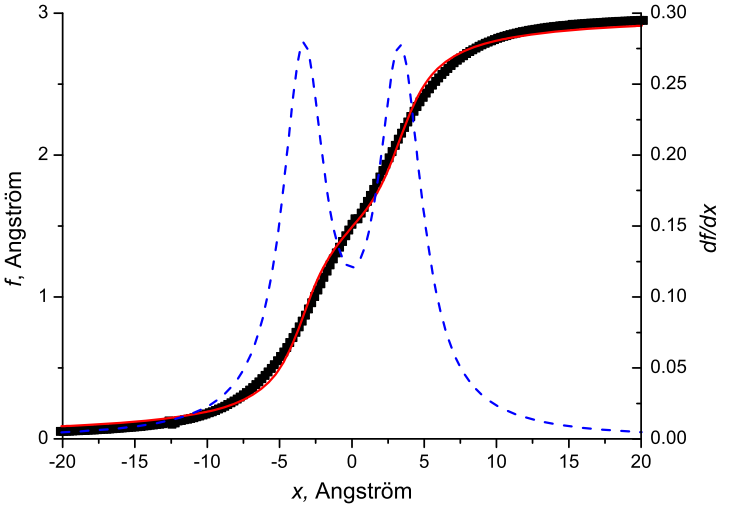

Figure 10. (colour online) Core structure of edge dislocation. Disregistry function *f(x)* and associated Burgers vector density $\rho = df(x)/dx$ (dotted line) are plotted in (0 0 0 1) plane.

Table 3. 0°, 30°, 60° and 90° dislocation core parameters controlling the spreading in (0 0 0 1) plane, and Peierls stress σ_p (in MPa). Half-widths of each partial (ξ_i) are given in Angstroms. The separation distances Δ (calculated value) and Δth (equilibrium distance according to anisotropic elasticity considering a staking fault energy of 0.72 J/m^2) between partials are expressed in Angstroms. a' is the periodicity of the misfit energy density.

Dislocation character	ξ_1	ξ_2	Δ	Δth	σ_p	a'
0°	1.8	1.9	5.26	3.22	611	$\frac{a_1\sqrt{3}}{2}$
30°	2.2	2.1	6.09	4.91	830	a_1
60°	1.7	1.9	6.58	6.28	957	$\frac{a_1\sqrt{3}}{2}$
90°	1.9	1.8	6.68	5.97	680	a_1

opposite side, the 60° character seems to be the hardest character to glide in the basal plane.

4. Discussion

In this study, we have used *ab initio* calculations to explore the γ-surfaces in the basal plane. We have considered the possibility of shearing the Ti_2AlN structure along the basal plane at two different levels. Shearing the (0 0 0 1) plane between Ti and N cut the Ti_6N octahedrons and induce higher values for the γ-surface energy than cutting between the Ti and Al atoms (which are more widely separated). This suggests that dislocations glide will occur preferentially in the basal plane between Ti and Al atoms. Therefore, in the studied dislocations core structures, we use only the (Ti–Al) γ-surface.

The second critical point to examine is the dislocation core structures. Whatever the character (screw, 30°, 60° and edge) all $\frac{1}{3}\langle\bar{2}\,1\,1\,0\rangle$ dislocations dissociate into two partial dislocations, with the dissociation scheme:

$$\frac{1}{3}\langle\bar{2}\,1\,1\,0\rangle \rightarrow \frac{1}{3}\langle\bar{1}\,1\,0\,0\rangle + \frac{1}{3}\langle\bar{1}\,0\,1\,0\rangle \tag{5}$$

This is the consequence of the stable stacking fault observed at $\frac{1}{3}\langle 1\,\bar{1}\,0\,0\rangle$ on the γ-surface. Figure 6 shows the dissociation path for $\frac{1}{3}\langle\bar{2}\,1\,1\,0\rangle$ dislocations, which is in good agreement with the expected path shown on Figure 3. The analysis of the dissociated configuration shows that each dislocation character dissociates into partials which have a character different from the perfect dislocation. The screw dislocation is dissociated into two 30° partials. The edge dislocation is dissociated into two 60° partials. The 30° and 60° dislocations are dissociated into two uneven partials. The 30° dislocation is dissociated into a screw and a 60° partials. The 60° dislocation is dissociated into an edge and a 30° partials.

As already mentioned, the splitting into partials results from the occurrence of a stable stacking fault configuration at $\frac{1}{3}\langle\bar{1}\,1\,0\,0\rangle$. The dissociation distance between partials depends thus on a competition between the staking fault energy of 0.72 J/m^2 and the anisotropic elastic forces acting on partial dislocations. Based on Stroh's theory [31,32], as implemented in DISDI software [33], equilibrium distances Δth between the partials can be evaluated (Table 3) considering anisotropic elasticity. It turns out that both theoretical distance Δth and PNG calculations are in good agreement with 60° and 90° dislocations exhibiting significantly larger dissociation distances. As Δ_{th} evaluation does not take into account the partial core spreading, the largest deviation (around 2 Å) between the two models is found for the initial screw core configuration. The advantage of the PNG calculations is thus to predict the splitting of the core accounting for both the anisotropic material behaviour and the dislocation partials width.

As shown in Table 3, the value of the equilibrium distance between the two partials is always too small for individual partial dislocations to be resolved by TEM where the resolution in weak-beam dark-field is of the order of few nanometres. These dislocations are thus expected to appear as perfect dislocations in the TEM: this is indeed what has been reported by all the previous TEM studies on MAX phases, notably by Guitton et al. [7] for the Ti_2AlN case.

Moreover, Guitton et al. [7] observed by TEM a tendency for the dislocations to adopt preferentially four main characters in the basal plane: screw, 30°, 60° and edge. At first glance, these observations could have been understood as an effect of a pronounced lattice friction. The Peierls stress values calculated for these four particular characters suggest that the 30° and 60° segments are the less mobile and would be thus more frequently observed in the TEM: this is not what has been reported in ref [7], where no predominance of any of the four characters has been observed. This present work complements the experimental observations of Guitton et al. [7] and constitutes a first step in the determination of the Peierls stress in MAX phases. In particular, it suggests that the preferential alignment of dislocations in the Ti_2AlN MAX phase is rather due to self-organization associated with elastic interactions between dislocations.

Second, these calculations show that dislocation glide in the basal plane will occur preferentially between M (here Ti) and A (here Al) planes. Even if this result is not

surprising, it can be helpful to predict the hardening effect expected in some MAX phase solid solutions. Indeed, substitution can be made on either M [34], A [35–37] or X sites [38], which leads, in some cases, to the improvement of hardness. A systematic study of the different possible M-A and M-X γ-surfaces would help in the prediction of possible effects of substitution or substoichiometry on the ease of dislocation glide in the basal plane.

Recent results in TEM observations of dislocations structures induced by high temperature compression have shown the activation of cross slip from the basal plane to both prismatic and pyramidal glide planes [39]. A next step would be thus to calculate the γ-surfaces and dislocations core structures in these newly evidenced slip planes.

Acknowledgements

The authors thank Christophe Denoual for helpful discussions and support in the PNG calculations. Computational resources have been provided by the CRI-Université de Lille 1.

Disclosure statement

No potential conflict of interest was reported by the authors.

Funding

This work was supported by the European Research Council under the Seventh Framework Programme (FP7), ERC [grant number 290424] – Rheoman.

References

[1] M.W. Barsoum, Prog. Solid State Chem. 28 (2000) p.201.
[2] J.C. Schuster, H. Nowotny and C. Vaccaro, J. Solid State Chem. 32 (1980) p.213.
[3] M.W. Barsoum and T. El-Raghy, Am. Sci. 89 (2001) p.334.
[4] M.W. Barsoum and M. Radovic, *Mechanical Properties of the MAX Phases, in Encyclopedia of Materials: Science and Technology* 2nd ed., K.H.J. Buschow, R.W. C, M.C. Flemings, B. Ilschner, E.J. Kramer, S. Mahajan and P. Veyssière, eds., Elsevier, Oxford, 2004, p.1.
[5] M.W. Barsoum, L. Farber and T. El-Raghy, Metall. Mater. Trans. A-Phys. Metall. Mater. Sci. 30 (1999) p.1727.
[6] Z.F. Zhang and Z.M. Sun, Mat. Sci. Eng.: A 408 (2005) p.64.
[7] A. Guitton, A. Joulain, L. Thilly and C. Tromas, Philos. Mag. 92 (2012) p.4536.
[8] C. Tromas, N. Ouabadi, V. Gauthier-Brunet, M. Jaouen and S. Dubois, J. Am. Ceram. Soc. 93 (2010) p.330.
[9] L. Farber, I. Levin, M.W. Barsoum, T. El-Raghy and T. Tzenov, J. Appl. Phys. 86 (1999) p.2540.
[10] A. Joulain, L. Thilly and J. Rabier, Philos. Mag. 88 (2008) p.1307.
[11] V. Vítek, Philos. Mag. 18 (1968) p.773.
[12] C. Denoual, Phy. Rev. B 70 (2004) p.024106.
[13] J.P. Perdew and Y. Wang, Phys. Rev. B 45 (1992) p.13244.
[14] G. Kresse and J. Furthmüller, Phys. Rev. B 54 (1996) p.11169.
[15] G. Kresse and J. Furthmüller, Comput. Mater. Sci. 6 (1996) p.15.
[16] G. Kresse and J. Hafner, Phys. Rev. B 47 (1993) p.558.

[17] P.E. Blöchl, Phys. Rev. B 50 (1994) p.17953.
[18] G. Kresse and D. Joubert, Phys. Rev. B 59 (1999) p.1758.
[19] H.J. Monkhorst and J.D. Pack, Phys. Rev. B 13 (1976) p.5188.
[20] D.C. Wallace, *Thermoelastic theory of stressed crystals and higher-order elastic constants*, in *Solid State Physics*, F.S. Henry Ehrenreich and T. David, eds., Academic Press, New York, 1970, p.301.
[21] M.F. Cover, O. Warschkow, M.M.M. Bilek and D.R. McKenize, J. Phys.-Condes. Matter. 21 (2009) p.305403.
[22] L. Pillon and C. Denoual, Philos. Mag. 89 (2009) p.127.
[23] L. Pillon, C. Denoual and Y.P. Pellegrini, Phys. Rev. B 76 (2007) p.224105.
[24] C. Denoual, Comp. Methods Appl. Mech. Eng. 196 (2007) p.1915.
[25] A. Bouhemadou, R. Khenata and M. Chegaar, Eur. Phys. J. B 56 (2007) p.209.
[26] G. Schoeck, Mater. Sci. Eng. A 400-401 (2005) p.7.
[27] G. Schoeck and M. Krystian, Philos. Mag. 85 (2005) p.949.
[28] D. Ferré, P. Carrez and P. Cordier, Phys. Chem. Miner. 36 (2009) p.233.
[29] T. Duong, S. Gibbons, R. Kinra and R. Arroyave, J. Appl. Phys. 110 (2011) p.093504.
[30] Z.J. Lin, M.J. Zhuo, M.S. Li, J.Y. Wang and Y.C. Zhou, Scr. Mater. 56 (2007) p.1115.
[31] G. Schoeck, Acta Mater. 45 (1997) p.2597.
[32] A. Stroh, Philos. Mag. 3 (1958) p.625.
[33] J. Douin, P. Veyssiere and P. Beauchamp, Phil. Mag. A 54 (1986) p.375.
[34] I. Salama, T. El-Raghy and M.W. Barsoum, J. Alloy. Compd. 347 (2002) p.271.
[35] S. Dubois, G.P. Bei, C. Tromas, V. Gauthier-Brunet and P. Gadaud, Int. J. Appl. Ceram. Technol. 7 (2010) p.719.
[36] W.B. Yu, S.B. Li and W.G. Sloof, Mater. Sci. Eng. A 527 (2010) p.5997.
[37] S.B. Li, W.B. Yu, H.X. Zhai, G.M. Song, W.G. Sloof and S. van der Zwaag, J. Eur. Ceram. Soc. 31 (2011) p.217.
[38] M.W. Barsoum and M. Radovic, *Elastic and mechanical properties of the MAX phases*, in *Annual Review of Materials Research*, Vol. 41, D.R. Clarke and P. Fratzl, eds., Annual Reviews, Palo Alto, CA 2011, p.195.
[39] A. Guitton, A. Joulain, L. Thilly and C. Tromas, Sci. Rep. 4 (2014) p.6358.
[40] W.Voigt, *Lehrbuch der Kristallphysik*, Teubner, Leipzig, 1928.
[41] B. Holm, R. Ahuja, S. Li and B. Johansson, J. Appl. Phys. 91 (2002) p.9874.